Pressure-driven 5*f* localized-itinerant transition and valence fluctuation in cubic phase californium

Li Huang* and Haiyan Lu
Science and Technology on Surface Physics and Chemistry Laboratory, P.O. Box 9-35, Jiangyou 621908, China

(Received 2 April 2018; revised manuscript received 5 December 2018; published 3 January 2019)

A combination of the density functional theory and the single-site dynamical mean-field theory is employed to study the pressure dependence of the electronic structure for cubic phase californium. We predict that its 5*f* electrons could undergo an orbital-selective localized-itinerant transition under moderate pressure. The volume contraction causes remarkable charge redistribution and valence fluctuation behaviors, which are the driving forces of the divalent-trivalent transition. Additionally, we find that the angular momentum coupling mechanism is hardly affected by pressure. The 5*f* orbital occupancy is well described by the intermediate-coupling scheme.

DOI: 10.1103/PhysRevB.99.045109

I. INTRODUCTION

The actinides are perhaps the most fascinating but least understood elements in the periodic table. They manifest a plethora of interesting physical properties, such as intricate *P*-*T* phase diagrams, low-symmetry crystal structures, multiple valence states, heavy-fermion features, and unconventional superconductivity, but only a few of them have been studied by experiments or theoretical calculations [1]. There is no doubt that the physical properties of the actinides are dominated by their electronic structures, specifically, the status of their 5*f* states. The 5*f* states are usually correlated. There exists a tricky interplay between Coulomb interaction, Hund's exchange, and spin-orbit coupling. The 5*f* states are also Janus faced; that is, they can evince either localized or itinerant characters depending on their surroundings [2]. The complex nature of the 5*f* states gives rise to extremely complicated electronic structures and unprecedentedly exotic physics.

Over the past decades, considerable attention has been given to the light and middle actinides. Of particular interest is plutonium, which locates at the nexus of an unusual ∼40% volume change that occurs in the actinides [3]. Clearly, the 5*f* states of Pu, which go from being delocalized to localized, should be responsible for the dramatic volume change and the other anomalous properties [4,5]. There have been extensive investigations concerning its magnetism [6–8], electronic structures [9–14], lattice dynamics [15–17], phase transitions, and phase stability [18–22]. On the contrary, the late actinides, such as americium, curium, berkelium, and californium, have received much less attention [22–29]. The reasons are twofold. On the one hand, these materials are toxic and radioactive, which makes handling them difficult and expensive. On the other hand, it is generally believed that their 5*f* states are highly localized at ambient pressure and scarcely contribute to the chemical bonding [27–29]. However, beyond the 5*f* localized-itinerant transition, we argue that these elements could present many intriguing physical properties under pressure. A typical example is Cf, whose cubic phase could provide an ideal test bed for investigating the complex behaviors of 5*f* states.

To our knowledge, Cf is the heaviest actinide on which lattice structure studies can be performed at present [1]. Recently, Heathman *et al.* studied the crystal structure of Cf up to 100 GPa by using both x-ray diffraction and theoretical calculations [30]. They observed four different crystallographic phases. At ambient conditions, Cf presents a mixture of Cf I (double hcp) and Cf II (fcc) phases. Then the mixture gradually converts to the Cf II phase under pressure. This transformation is completed at about 14 GPa. Upon additional pressure, the Cf II phase converts to another mixture of Cf III (face-centered orthorhombic) and Cf IV (base-centered orthorhombic) phases, which emerges at about 35 GPa and is retained at least up to 100 GPa. Note that the volume collapse during the II-III transition is about 4.8%, and that during the II-IV transition is about 15%, which is attributed to the delocalization of the 5*f* states again. Cf is also the only actinide to exhibit more than one valence (viz., divalent, intermediate-valence, and trivalent states) at near-ambient conditions [1]. Previously, theoretical calculations of its 5*f*-6*d* promotion energy suggested that Cf falls into the boundary region between divalent and trivalent metallic bonding [31,32]. Recent experiments confirmed that its divalent state is metastable, which will transform into the intermediate-valence state and then the trivalent state under moderate pressure [30].

Prior to experiments, the Cf III and Cf IV phases were successfully predicted by using density functional theory. However, this method has difficulty describing the correlated nature of Cf's 5*f* electrons (see the Appendices A and B). In the present work, we employ a state-of-the-art first-principles many-body approach, namely, a combination of density functional theory and single-site dynamical mean-field theory (dubbed DFT + DMFT) [33,34], to study the electronic structure of the cubic Cf II phase under pressure. This approach has been widely used to study the electronic structures and related physical properties of Pu, Am, Cm, and many other actinide-based materials [7–15]. Our results suggest that external pressure can tune the 5*f* states in a subtle manner. Several fascinating effects are predicted in cubic phase Cf, such as the orbital-selective 5*f* localized-itinerant

*lihuang.dmft@gmail.com

transition, divalent-trivalent transition, restricted valence state fluctuation, and collapse of the local magnetic moment.

II. METHODS

The DFT calculations are done using the WIEN2K code, which implements the full-potential linear augmented plane-wave (FP-LAPW) formalism [35]. The cutoff parameter is $R_{\mathrm{MT}}K_{\mathrm{MAX}} = 7.0$. The muffin-tin radius for the Cf atom is fixed at 2.5 bohrs. The spin-orbit coupling is always considered in the calculations. We choose the generalized gradient approximation (i.e., the revised Perdew-Burke-Ernzerhof functional) to express the exchange-correlation potential [36–38]. The Brillouin zone integration is done on a uniform $17 \times 17 \times 17$ k mesh (165 k points in the first irreducible Brillouin zone). During the calculations the crystal symmetry is kept, but the lattice constants are rescaled to mimic the effect of external pressure.

We employ the EDMFTF software package developed by Haule *et al.* [39] to perform the charge fully self-consistent DFT + DMFT calculations. About 50 DFT + DMFT cycles are enough to obtain converged results. The convergence criteria for charge and total energy are 10^{-4} e and 10^{-4} Ry, respectively. Each DFT + DMFT cycle contains a one-shot DMFT calculation and a maximum of 40 DFT calculations. The inverse temperature $\beta = 40.0$ (the corresponding temperature T is about 290 K, which is much larger than the antiferromagnetic Néel temperature $T_N = 48$–66 K). We make the system be paramagnetic. The $5f$ bands of the Cf atom are treated as correlated. The Coulomb interaction matrix is constructed through the Slater integrals [40]. The Coulomb interaction parameter $U = 7.0$ eV, and the Hund's exchange parameter $J_H = 0.7$ eV, which are taken from Ref. [1] directly (see Appendix C). The double-counting term for the self-energy function is described by the fully localized limit (FLL) scheme [41]:

$$\Sigma_{\mathrm{dc}} = U\left(n_{5f} - \frac{1}{2}\right) - \frac{J_H}{2}(n_{5f} - 1), \tag{1}$$

where n_{5f} is the $5f$ occupation number, which should be adjusted dynamically during the iterations. We utilize the hybridization expansion continuous-time quantum impurity solver (dubbed CT-HYB) to solve the resulting 14-orbital Anderson impurity models [42,43]. The number of Monte Carlo sweeps is about 2×10^8. In order to improve the computational efficiency, we truncate the Hilbert space of the atomic Hamiltonian. Only those atomic eigenstates with $N \in [8, 11]$ are kept. Furthermore, the lazy trace evaluation trick is adopted [44]. Once the DFT + DMFT iteration is finished, we adopt the maximum entropy method to perform analytical continuation for the Matsubara self-energy function [45]. And then the obtained real-frequency self-energy function is used to evaluate the other physical observables, such as momentum-resolved spectral functions $A(\mathbf{k}, \omega)$ and density of states $A(\omega)$.

III. RESULTS AND DISCUSSION

A. Orbital-selective $5f$ localized-itinerant transition

First, we calculate the spectral functions of cubic phase Cf with respect to various pressures (or lattice constants a_0). We concentrate on the momentum-resolved spectral functions $A(\mathbf{k}, \omega)$, the total density of states $A(\omega)$, and the $5f$ partial density of states $A_{5f}(\omega)$, which are depicted in Figs. 1(a) and 1(b), respectively. The results endorse the scenario of pressure-driven electronic Lifshitz transition, which could be divided into three different stages. (i) In the first stage, $a_0 > 9.6$ bohrs. There are stripelike band structures in the momentum-resolved spectral functions, which are associated with the $5f$ states. These bands are nearly flat and far away from the Fermi level, indicating the localized nature of the $5f$ states. The $5f$ partial density of states shows obviously insulating behavior. When $a_0 = 10.2$ bohrs, the $5f$ band gap is estimated to be 3.0 eV. (ii) Next, $a_0 \sim 9.6$ bohrs. The occupied $5f$ bands are shifted toward the Fermi level. As a consequence, the $5f$ band gap is greatly reduced. (iii) Finally, $a_0 < 9.6$ bohrs. A strong quasiparticle peak emerges at the Fermi level, which is attributed to the itinerant $5f$ states. The $5f$ band gap is completely closed. We thus speculate that there is a small-to-large Fermi surface transition, accompanied by a change in the Fermi surface topology [46,47].

Then we focus on the hybridization functions $\Delta(\omega)$, which are generally used to measure the hybridization strength between the correlated $5f$ and noncorrelated spd bands. Figure 1(c) depicts the imaginary parts of hybridization functions. The $5f$-spd hybridization mostly takes place at the unoccupied states. However, when $a_0 < 9.6$ bohrs, a sizable spectral weight transfers from unoccupied to occupied states. All these features suggest that under pressure, the $5f$ states in Cf should undergo a typical localized-itinerant transition. According to the experimental P-V curve [30], the transition will happen around 10 GPa. Note that similar transitions have already been observed at the high-pressure phases of Am and Cm [26–29].

Let's analyze this localized-itinerant transition further. Due to the spin-orbit coupling, the $5f$ orbitals can be split into the $5f_{5/2}$ and $5f_{7/2}$ subbands. The most astonished thing is that the localized-itinerant transitions do not occur simultaneously for the $5f_{5/2}$ and $5f_{7/2}$ states. In Fig. 1(d), the $5f$ band gap as a function of lattice constants is plotted. When $a_0 < 9.6$ bohrs (or $a_0 > 9.7$ bohrs), both the $5f_{5/2}$ and $5f_{7/2}$ states are metallic (or insulating). However, in the intermediate regime (i.e., 9.6 bohrs $< a_0 <$ 9.7 bohrs), the $5f_{7/2}$ states become metallic while the $5f_{5/2}$ states still retain insulating. In order to confirm the coexistent zone, we further calculate $\beta|G(\tau = \beta/2)|$, which is in proportion to $A(\omega = 0)$ when $\beta \to \infty$ [48]. The calculated results are quite similar, as seen in Fig. 1(e). Therefore, we believe that this localized-itinerant transition is orbital selective, which is an analogy to the orbital-selective Mott insulator-metal transition for multiorbital correlated electron systems [49,50].

B. Valence state transition and charge redistribution

As mentioned before, a valence state transition (divalent-trivalent) would take place upon volume compression [30–32]. Previous studies suggested that the low $5f$-$6d$ promotion energy will facilitate this transition, but the underlying mechanism remains unclear so far. In the present work, we investigate the pressure-driven charge fluctuation and find some useful clues. First, even if the structural transition is

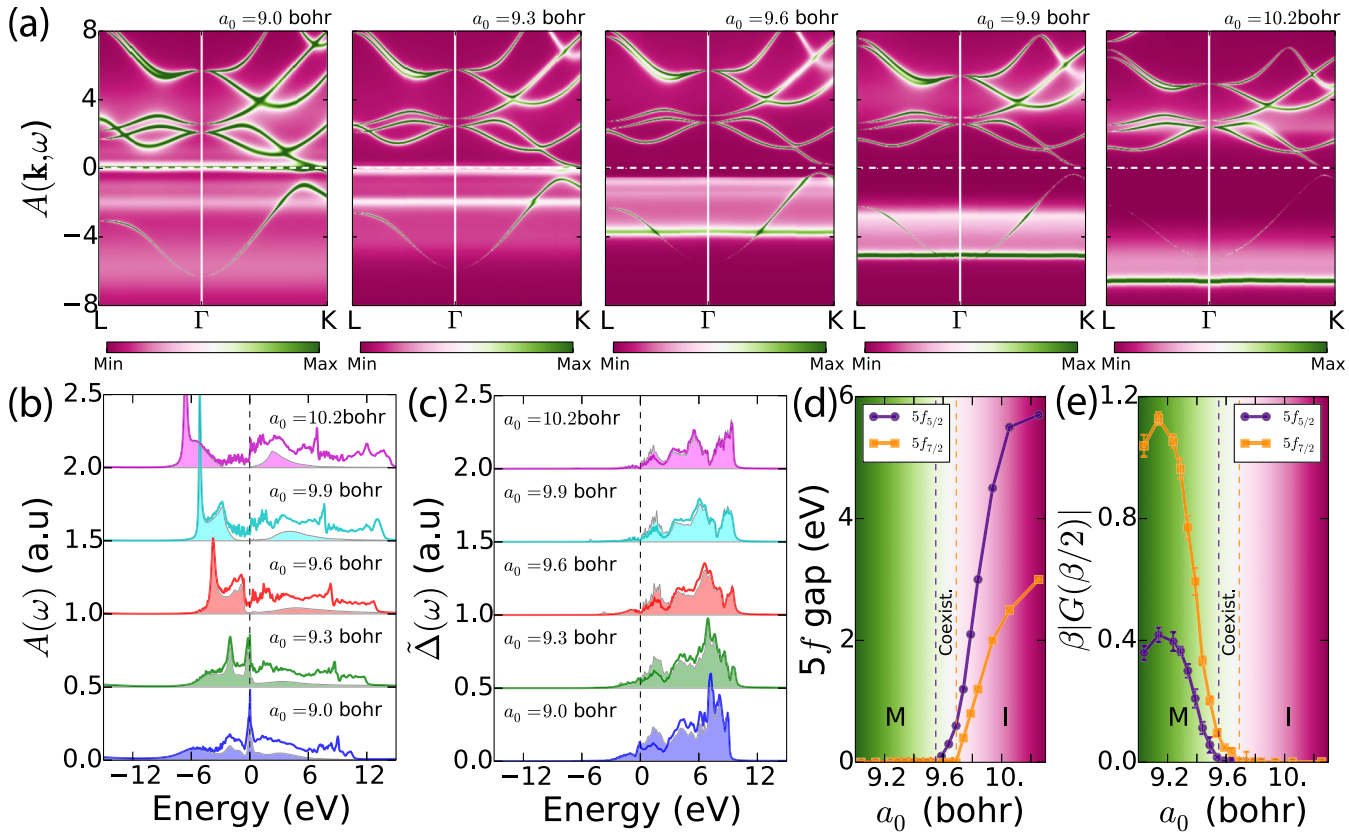

FIG. 1. Pressure-dependent electronic structures of cubic phase Cf. (a) Momentum-resolved spectral functions $A(\mathbf{k},\omega)$. The horizontal lines denote the Fermi level. (b) Total density of states $A(\omega)$ (thick solid lines) and 5f partial density of states $A_{5f}(\omega)$ (color-filled regions). (c) Imaginary parts of hybridization functions $\tilde{\Delta}(\omega) = -\mathrm{Im}\Delta(\omega)/\pi$. The $5f_{5/2}$ and $5f_{7/2}$ components are represented by thick solid lines and color-filled regions, respectively. (d) The 5f band gap as a function of lattice constants. (e) $\beta|G(\tau=\beta/2)|$ as a function of lattice constants, where $G(\tau)$ is the imaginary-time Green's function for 5f orbitals and $\beta = 1/T$ is the inverse temperature. In (d) and (e), the letters "M" and "I" mean metallic and insulating characters, respectively.

ignored and only the Cf II phase is considered, we can reproduce the valence state transition [see Fig. 2(a)]. Second, the 5f electrons are mainly promoted to the 6d orbitals, but the electron transfer from 5f to 6p (or 7s) orbitals cannot be neglected [see Fig. 2(b)]. Third, the charge fluctuation χ_c reaches its local maxima at $a_0 \sim 9.3$ bohrs [see Fig. 2(c)]. Growing the 5f-spd hybridization and the crossover of $5f^{10}$ and $5f^9$ levels may explain this peak. Since χ_c is proportional to the system's compressibility [33], it is reasonable to predict that this maximum leads to softening of the entire electronic liquid, which will manifest in the P-V curve of Cf, in analogy to the fluctuating valence metal Yb [51].

C. Valence state transition and atomic eigenstates fluctuation

The valence state histogram p_Γ represents the probability to find a valence electron in a given atomic eigenstate $|\psi_\Gamma\rangle$, which is, in general, labeled by assorted good quantum numbers, such as N (occupancy), J (total angular momentum), and γ (which stands for the rest of the good quantum numbers). It is a versatile tool to study the electronic configurations of realistic materials [8,9]. In Figs. 3(a)–3(c), the valence state histograms for three typical cases ($a_0 = 9.0$, 9.6, and 10.2 bohrs) are shown. The corresponding distributions of 5f atomic eigenstates with respect to N are illustrated in Figs. 3(d)–3(f). When $a_0 = 10.2$ bohrs, the atomic eigenstate fluctuation is very weak. The 5f electrons are virtually locked into the $5f^{10}$ configuration, and the valence state histogram is peaked only at the ground state of the atom (i.e., $|N = 10, J = 8, \gamma = 0\rangle$). Cf behaves like a divalent metal (valence ~2.0, $n_{5f} \sim 10.0$). When $a_0 = 9.6$ bohrs, the atomic eigenstate fluctuation becomes significant. Although the $5f^{10}$ configuration remains predominant, the contributions from the $5f^9$ configuration are not trivial. As a result, Cf begins to exhibit mixed-valence properties (valence ~2.2, $n_{5f} \sim 9.8$). When $a_0 = 9.0$ bohrs, the dominant atomic eigenstate is $|N = 9, J = 7.5, \gamma = 0\rangle$, which is also the ground state of the atom. The atomic eigenstate $|N = 10, J = 8, \gamma = 0\rangle$ becomes less important. It appears that the 5f electrons live a double life, spending nearly all their time in the two states. In other words, the atomic eigenstate fluctuation involves only two principal states. The other atomic eigenstates are practically excluded. We call this behavior "restricted atomic eigenstate fluctuation," which distinguishes Cf from the other typical mixed-valence materials, such as Pu [8,9]. At this moment, Cf is nearly a trivalent metal (valence ~2.7, $n_{5f} \sim 9.3$). Figure 3(g) shows the probabilities for the $5f^8$-$5f^{11}$ configurations. The probabilities for the $5f^{10}$ configuration increase monotonously against the lattice constants, while the trends for the other configurations are the opposite. In addition, we

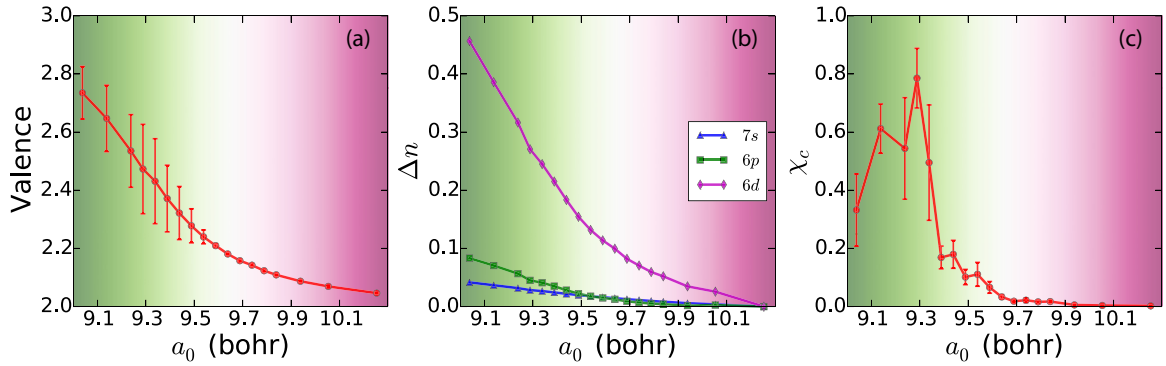

FIG. 2. Valence state transition in cubic phase Cf upon volume compression. (a) Valence. The data are evaluated via the formula valence $= 12 - n_{5f}$, where n_{5f} is the $5f$ orbital occupancy. (b) Number of electrons promoted from $5f$ to spd orbitals. (c) Charge fluctuation $\chi_c = (\langle n_{5f}^2 \rangle - \langle n_{5f} \rangle^2)/\beta$.

find that there is a cross of the $5f^{10}$ and $5f^9$ configurations at $a_0 \sim 9.3$ bohrs, which is related to the local maxima spotted in the local charge fluctuation χ_c. Accordingly, we believe that the charge redistribution and atomic eigenstate fluctuation are probably the driving forces of the divalent-trivalent transition.

Apart from the valence and $5f$ occupancy, it is also helpful to study the evolution of the other physical quantities with respect to the lattice constants. We try to calculate the averaged total angular momentum J_{av} via the following equation: $J_{\text{av}} = \sum_\Gamma p_\Gamma J_\Gamma$, where J_Γ denotes the total angular momentum of the atomic eigenstate $|\psi_\Gamma\rangle$. The results are plotted at Fig. 3(h). As is expected, we observe sizable collapse for J_{av} under pressure. Note that J_{av} declines more quickly when $a_0 <$ 9.6 bohrs. Since J_{av} is tightly connected to the local magnetic moment μ, it is plausible to suspect that μ will exhibit the same tendency, which is similar to the high-spin to low-spin transition in multiorbital Mott systems [52].

D. $5f$ orbital occupancy and angular momentum coupling

As is well known, there are two standard ways to couple the angular momenta of multielectronic systems: Russell-Saunders (LS) and jj coupling. Provided that the spin-orbit coupling is weak compared to the electrostatic interactions, the LS coupling is favorable, or else the jj coupling wins [1]. As for the actinides, however, both the spin-orbit

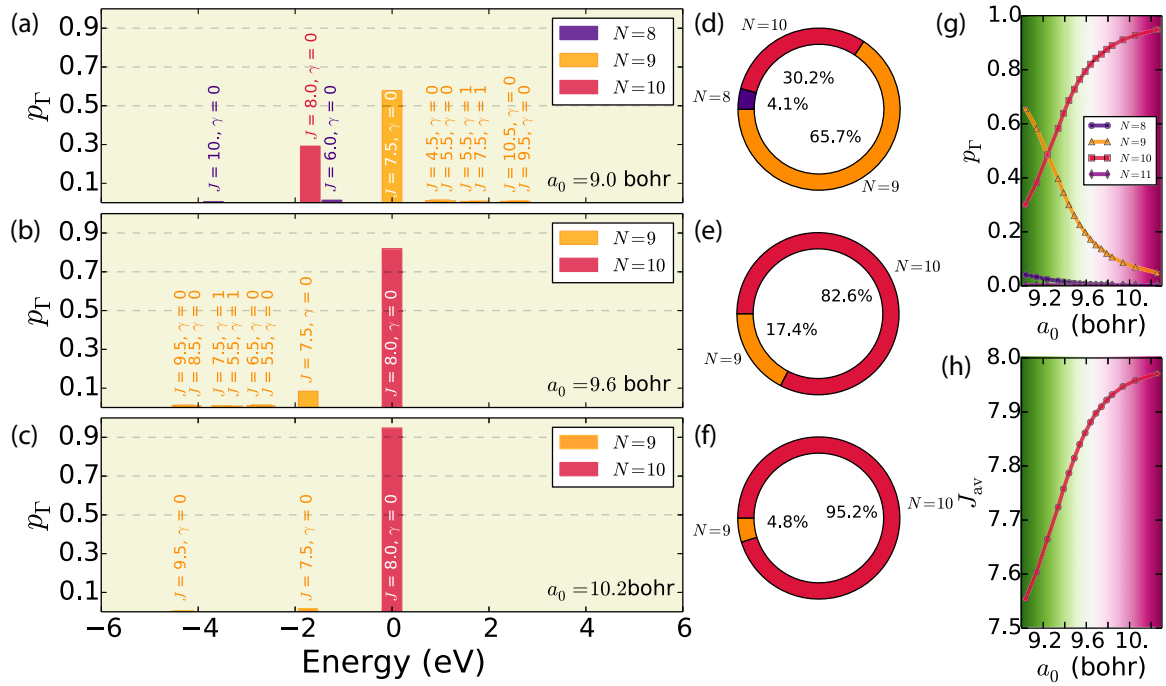

FIG. 3. Valence state fluctuation in cubic phase Cf upon volume compression. (a)–(c) Probabilities of the $5f$ atomic eigenstates (or, equivalently, valence state histograms) for various lattice volumes. (d)–(f) Distributions of $5f$ atomic eigenstates with respect to N for various lattice volumes. In these panels, only the contributions from the $N = 8$, 9, and 10 atomic eigenstates are shown. The contributions from the other atomic eigenstates are too trivial to be seen. (g) Distributions of $5f$ atomic eigenstates with respect to volume compression. (h) Averaged total angular momentum J_{av} as a function of lattice constants.

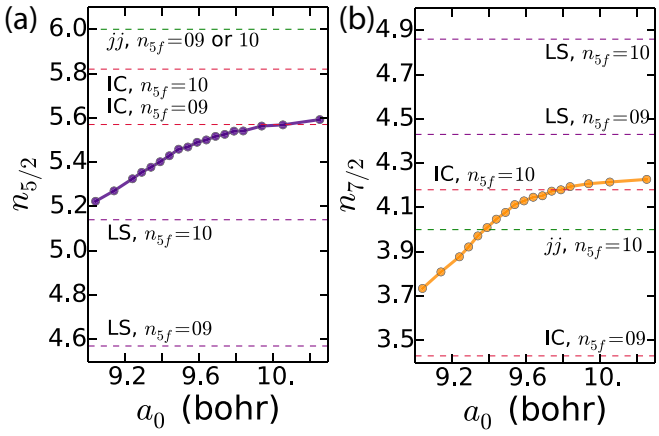

FIG. 4. The 5f orbital occupancy of cubic phase Cf upon volume compression for (a) the $n_{5/2}$ case and (b) the $n_{7/2}$ case. The horizontal dashed lines denote the theoretical values deduced by using various angular momentum coupling schemes (i.e., LS, IC, and jj) [1]. As $n_{5f} = 09$ and the jj-coupling scheme is adopted, the theoretical value for $n_{7/2}$ is 3, which is not shown in (b).

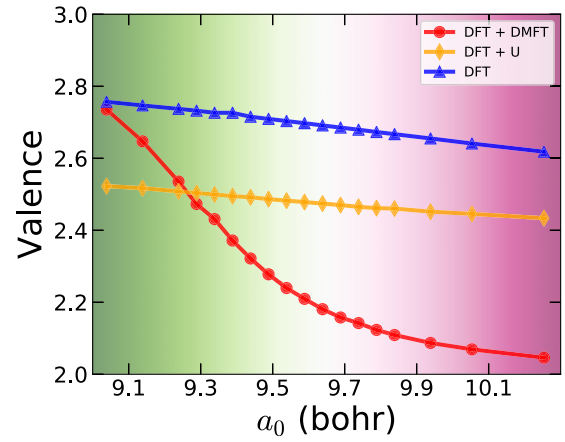

FIG. 5. Valence state transition in cubic phase Cf upon volume compression. The data are evaluated via the formula valence $= 12 - n_{5f}$, where n_{5f} is the 5f orbital occupancy.

coupling and the electrostatic interactions are important. In this regard, the intermediate-coupling (IC) scheme which takes both interactions into account is more appropriate [53]. One exception to this rule is uranium, which exhibits LS coupling. What's the angular momentum coupling scheme for Cf? Will it change under pressure? In order to answer these questions, we calculate its 5f orbital occupancy (see Fig. 4). The calculated values obviously favor the IC scheme. For example, given that $n_{5f} \sim 10.0$ ($a_0 = 10.2$ bohrs), the calculated $n_{7/2}$ is approximately 4.23 [54]. However, the theoretical occupation numbers for $5f_{7/2}$ states are 4.86, 4.0, and 4.18 for the LS, jj, and IC coupling schemes, respectively. The corresponding errors are 14.9%, −5.4%, and −1.2%, respectively. Hence, we infer that the IC scheme still holds for Cf at ambient conditions. Furthermore, the angular momentum coupling scheme will not change over the entire pressure (or volume) range of interest. Because the 5f orbital occupancy can be used to calculate the x-ray branching ratio, the electron energy-loss spectroscopy and x-ray absorption spectroscopy can be employed to validate our results.

IV. CONCLUSIONS

We have examined the pressure-driven 5f localized-itinerant transition and valence fluctuation in cubic phase Cf by using the DFT + DMFT approach. We believe that the 5f localized-itinerant transition is orbital selective. There exists a considerable volume range where the insulating $5f_{5/2}$ state and the metallic $5f_{7/2}$ state could coexist. We also interpret the divalent-trivalent transition as a result of charge redistribution and valence state fluctuation. The valence state fluctuation is greatly restricted. It mainly involved two atomic eigenstates, in contrast to common fluctuating valence materials. Perhaps most importantly we confirm that Cf still obeys the IC scheme, which is not affected by pressure. Our results reveal that the 5f electronic structures for the late actinides under pressure are very interesting. Further theoretical and experimental investigations are highly desired.

ACKNOWLEDGMENTS

This work was supported by the Natural Science Foundation of China (Grants No. 11874329, No. 11504340, and No. 11704347), the Foundation of the President of China Academy of Engineering Physics (Grant No. YZ2015012), and the Science Challenge Project of China (Grant No. TZ2016004).

APPENDIX A: DFT + U COMPUTATIONAL DETAILS

As a cross-check for the DFT + DMFT results, we perform additional DFT + U calculations. The DFT + U calculations are done by using the WIEN2K code. The spin polarization is allowed, and spin-orbit coupling is included. We choose the scheme proposed by Anisimov *et al.* [55] to treat the Hubbard interaction. The chosen interaction parameters are the same as those used in the DFT + DMFT calculations, namely, $U =$ 7.0 eV and $J_H = 0.7$ eV. But in the DFT + U calculations, we set $U_{\text{eff}} = U - J_H$, and $J_{\text{eff}} = 0.0$ eV.

APPENDIX B: RESULTS OF THE DFT AND DFT + U METHODS

We apply the DFT and DFT + U methods to examine the valence state transition in cubic phase Cf upon volume compression. The calculated results, together with those obtained with the DFT + DMFT results, are shown in Fig. 5. Clearly, although the mixed-valence behavior is correctly reproduced, both methods do not support the scenario of (hypothetical) valence state transition, in contrast to the DFT + DMFT method.

APPENDIX C: FREQUENCY-DEPENDENT AND PRESSURE-DEPENDENT INTERACTIONS

Generally speaking, the strengths of Coulomb repulsion interaction and Hund's exchange interaction should depend on the lattice volume (or pressure) explicitly. However, for the sake of simplicity, we chose constant U and J_H parameters in our DFT + U and DFT + DMFT calculations. It is

unclear whether this assumption is valid or not. To answer this question, we have to determine U and J_H by ourselves.

To our knowledge, there are usually two different methods to calculate U and J_H, namely, the constrained local-density approximation [56–58] and constrained random-phase approximation (cRPA) [59–62]. The cRPA method relies on the linear response theory to compute the screened interaction. Screening processes corresponding to electron-hole transitions among the correlated orbitals are excluded from the calculation. The advantages of the cRPA method are twofold. First, it can provide frequency-dependent (or energy-dependent) interaction parameters. Not only on-site U but also off-site U can be calculated. It is straightforward to obtain U and J_H in their matrix forms. Second, the cRPA method has been implemented in many first-principle codes. It was applied to different strongly correlated systems in the past few years. In the present work, we use the cRPA method to study the evolution of U and J_H parameters for cubic phase Cf with respect to lattice constants. Unfortunately, up to now the cRPA method has not been implemented in the WIEN2K code. Thus, we turn to the ABINIT code, which implements the pseudopotential plane-wave formalism [63,64]. Note that Amadon *et al.* implemented the self-consistent cRPA method [61] in this code a few years ago. Later, they applied this feature to study the effective Coulomb interactions of some actinide elements, and then they utilized these parameters to conduct successive DFT + DMFT calculations [62]. The calculated results are quite impressive.

Inspired by Amadon *et al.*'s works, we follow the following procedures to do the calculations.

(i) *Construction of the pseudopotential*. First, a reliable projector augmented-wave (PAW) data set (i.e., pseudopotential) [65] for Cf is essential. Because there is no available PAW data set for Cf, we have to create it ourselves. We use the ATOMPAW code [66] to achieve this goal. The electronic configuration for Cf is [Rn]$5f^{10}7s^2$. The $6s$ orbital is treated as a semicore state. The total number of valence electrons is 30 ($5d^{10}5f^{10}6s^26p^67s^2$). The scalar-relativistic effect is included in the atomic all-electron calculation. We choose Blöchl's scheme [65] to generate smooth pseudo partial waves $\tilde{\phi}_i$ and the associated projectors $\tilde{p}_i$. The atomic potential is pseudized to generate local pseudopotential V_{loc} within the Troullier-Martins scheme. The radius of augmentation regions in PAW formalism r_{PAW} is 2.3. In order to help others reproduce our results, this PAW data set has been released through GitHub. It can be downloaded and used freely [67].

(ii) *DFT calculation*. We carry out the self-consistent DFT calculation with the ABINIT code. The kinetic energy cutoff which controls the number of plane waves is 15 Ha. The k points are defined on a $4 \times 4 \times 4$ Monkhorst-Pack grid.

(iii) *cRPA calculation*. In the cRPA calculations, we have to define two energy (or band) windows. The outer window is used to construct local Wannier orbitals, which are unitarily related to a selected set of Kohn-Sham wave functions. The inner window is related to the constrained polarizability calculations. The electron-hole transitions inside this window will not be taken into consideration. In the present work, we just define the two windows by specifying the band indexes, instead of giving an energy range. The band indexes for the outer and inner windows are [10,28] and [10,18], respectively. The energy cutoffs for the calculations of the dielectric function and bare interaction are 10 and 30 Ha, respectively. As mentioned before, we can calculate frequency-dependent interaction parameters, namely, $U(\omega)$ and $J_H(\omega)$. A linear frequency mesh is defined between 0.0 and 20.0 eV. The number of frequency points is 200. When $\omega = 0.0$ eV, the static values are what we need.

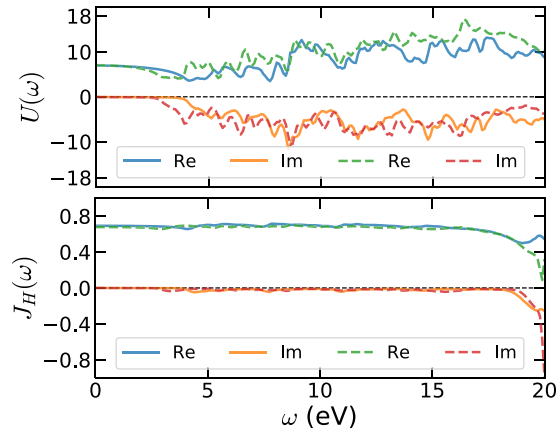

FIG. 6. Top: Frequency-dependent Coulomb interaction $U(\omega)$. Bottom: Frequency-dependent Hund's exchange interaction $J_H(\omega)$. Here, we consider two different cases: $a_0 = 9.0$ bohrs and $a_0 = 10.2$ bohrs. Their data are represented as solid and dashed lines, respectively.

The cRPA calculated results are as follows.

First, we obtain frequency-dependent U and J_H for cubic phase Cf at various volumes. In Fig. 6, we show two typical cases: $a_0 = 9.0$ bohrs and $a_0 = 10.2$ bohrs. We find that $U(\omega)$ is very sensitive to the change in volume. On the contrary, $J_H(\omega)$ is almost featureless, especially in the low-frequency regime. What's the role played by the frequency-dependent U in the localized-itinerant transition and divalent-trivalent transition? This is an interesting and unsolved question. We would like to dive into it in the future.

Next, we can extract static values from the dynamical U and J_H. They are the so-called screened interactions. The

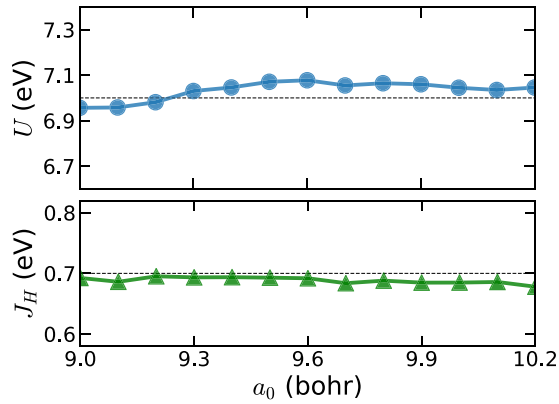

FIG. 7. Top: Volume-dependent Coulomb interaction U. Bottom: Volume-dependent Hund's exchange interaction J_H. The dashed lines denote the interaction parameters used in our DFT + U and DFT + DMFT calculations.

results are shown in Fig. 7. Clearly, the volume (or pressure) dependences of U and J_H are very weak. For example, when a_0 goes from 9.0 to 10.2 bohrs (+12%), U changes only from 6.95 to 7.04 eV (+1.3%). The asymptotic values of U and J_H are around 7.0 and 0.7 eV, respectively. They are very consistent with the values used in the DFT + U and DFT + DMFT calculations. Note that we also perform a lot of benchmark calculations by varying the kinetic energy cutoff, k-mesh density, inner and outer windows, and the other computational parameters. Although the asymptotic values of U and J_H are somewhat different (they strongly depend on the choice of inner and outer windows), the weak volume (or pressure) dependences always hold. This trend is obtained by using the ABINIT code, but we believe that its validity does not depend on the specific code or local basis; that is, it should be valid for the WIEN2K code as well.

In summary, the volume (or pressure) dependences of U and J_H are rather weak. This trend is correct at least at the range of volume (or pressure) we are interested in. Thus, it is reasonable to use fixed U and J_H in the DFT + U and DFT + DMFT calculations.

[1] K. T. Moore and G. van der Laan, Rev. Mod. Phys. **81**, 235 (2009).
[2] B. Johansson, Phys. Rev. B **11**, 2740 (1975).
[3] R. C. Albers, Nature (London) **410**, 759 (2001).
[4] J. Joyce, J. Wills, T. Durakiewicz, M. Butterfield, E. Guziewicz, D. Moore, J. Sarrao, L. Morales, A. Arko, O. Eriksson, A. Delin, and K. Graham, Physica B (Amsterdam, Neth.) **378-380**, 920 (2006).
[5] B. R. Cooper, P. Thayamballi, J. C. Spirlet, W. Müller, and O. Vogt, Phys. Rev. Lett. **51**, 2418 (1983).
[6] J. C. Lashley, A. Lawson, R. J. McQueeney, and G. H. Lander, Phys. Rev. B **72**, 054416 (2005).
[7] J. H. Shim, K. Haule, S. Savrasov, and G. Kotliar, Phys. Rev. Lett. **101**, 126403 (2008).
[8] M. Janoschek, P. Das, B. Chakrabarti, D. L. Abernathy, M. D. Lumsden, J. M. Lawrence, J. D. Thompson, G. H. Lander, J. N. Mitchell, S. Richmond, M. Ramos, F. Trouw, J.-X. Zhu, K. Haule, G. Kotliar, and E. D. Bauer, Sci. Adv. **1**, e1500188 (2015).
[9] J. H. Shim, K. Haule, and G. Kotliar, Nature (London) **446**, 513 (2007).
[10] J.-X. Zhu, R. C. Albers, K. Haule, G. Kotliar, and J. M. Wills, Nat. Commun. **4**, 2644 (2013).
[11] S. Y. Savrasov, G. Kotliar, and E. Abrahams, Nature (London) **410**, 793 (2001).
[12] C. A. Marianetti, K. Haule, G. Kotliar, and M. J. Fluss, Phys. Rev. Lett. **101**, 056403 (2008).
[13] L. V. Pourovskii, G. Kotliar, M. I. Katsnelson, and A. I. Lichtenstein, Phys. Rev. B **75**, 235107 (2007).
[14] E. Gorelov, J. Kolorenč, T. Wehling, H. Hafermann, A. B. Shick, A. N. Rubtsov, A. Landa, A. K. McMahan, V. I. Anisimov, M. I. Katsnelson, and A. I. Lichtenstein, Phys. Rev. B **82**, 085117 (2010).
[15] X. Dai, S. Y. Savrasov, G. Kotliar, A. Migliori, H. Ledbetter, and E. Abrahams, Science **300**, 953 (2003).
[16] R. J. McQueeney, A. C. Lawson, A. Migliori, T. M. Kelley, B. Fultz, M. Ramos, B. Martinez, J. C. Lashley, and S. C. Vogel, Phys. Rev. Lett. **92**, 146401 (2004).
[17] J. Wong, M. Krisch, D. L. Farber, F. Occelli, A. J. Schwartz, T.-C. Chiang, M. Wall, C. Boro, and R. Xu, Science **301**, 1078 (2003).
[18] K. T. Moore, P. Söderlind, A. J. Schwartz, and D. E. Laughlin, Phys. Rev. Lett. **96**, 206402 (2006).
[19] P. Söderlind and B. Sadigh, Phys. Rev. Lett. **92**, 185702 (2004).
[20] P. Söderlind, A. Landa, J. E. Klepeis, Y. Suzuki, and A. Migliori, Phys. Rev. B **81**, 224110 (2010).
[21] N. Lanatà, Y. Yao, C.-Z. Wang, K.-M. Ho, and G. Kotliar, Phys. Rev. X **5**, 011008 (2015).
[22] P. Söderlind, J. Electron Spectrosc. Relat. Phenom. **194**, 2 (2014).
[23] A. Lindbaum, S. Heathman, K. Litfin, Y. Méresse, R. G. Haire, T. Le Bihan, and H. Libotte, Phys. Rev. B **63**, 214101 (2001).
[24] S. Y. Savrasov, K. Haule, and G. Kotliar, Phys. Rev. Lett. **96**, 036404 (2006).
[25] J.-C. Griveau, J. Rebizant, G. H. Lander, and G. Kotliar, Phys. Rev. Lett. **94**, 097002 (2005).
[26] S. Heathman, R. G. Haire, T. Le Bihan, A. Lindbaum, M. Idiri, P. Normile, S. Li, R. Ahuja, B. Johansson, and G. H. Lander, Science **309**, 110 (2005).
[27] H. L. Skriver, O. K. Andersen, and B. Johansson, Phys. Rev. Lett. **41**, 42 (1978).
[28] H. L. Skriver, O. K. Andersen, and B. Johansson, Phys. Rev. Lett. **44**, 1230 (1980).
[29] S. Heathman, R. G. Haire, T. Le Bihan, A. Lindbaum, K. Litfin, Y. Méresse, and H. Libotte, Phys. Rev. Lett. **85**, 2961 (2000).
[30] S. Heathman, T. Le Bihan, S. Yagoubi, B. Johansson, and R. Ahuja, Phys. Rev. B **87**, 214111 (2013).
[31] B. Johansson, J. Phys. Chem. Solids **39**, 467 (1978).
[32] B. Johansson, Phys. Rev. B **19**, 6615 (1979).
[33] A. Georges, G. Kotliar, W. Krauth, and M. J. Rozenberg, Rev. Mod. Phys. **68**, 13 (1996).
[34] G. Kotliar, S. Y. Savrasov, K. Haule, V. S. Oudovenko, O. Parcollet, and C. A. Marianetti, Rev. Mod. Phys. **78**, 865 (2006).
[35] P. Blaha, K. Schwarz, G. K. H. Madsen, D. Kvasnicka, J. Luitz, R. Laskowski, F. Tran, and L. D. Marks, *WIEN2k: An Augmented Plane Wave + Local Orbitals Program for Calculating Crystal Properties*, edited by K. Schwarz (Karlheinz Schwarz, Techn. Universität Wien, Austria, 2018).
[36] J. P. Perdew, K. Burke, and M. Ernzerhof, Phys. Rev. Lett. **77**, 3865 (1996).
[37] J. P. Perdew, A. Ruzsinszky, G. I. Csonka, O. A. Vydrov, G. E. Scuseria, L. A. Constantin, X. Zhou, and K. Burke, Phys. Rev. Lett. **100**, 136406 (2008).
[38] J. P. Perdew, A. Ruzsinszky, G. I. Csonka, O. A. Vydrov, G. E. Scuseria, L. A. Constantin, X. Zhou, and K. Burke, Phys. Rev. Lett. **102**, 039902(E) (2009).
[39] K. Haule, C.-H. Yee, and K. Kim, Phys. Rev. B **81**, 195107 (2010).
[40] T. Fujiwara and M. Korotin, Phys. Rev. B **59**, 9903 (1999).

[41] V. I. Anisimov, F. Aryasetiawan, and A. I. Lichtenstein, J. Phys.: Condens. Matter **9**, 767 (1997).

[42] K. Haule, Phys. Rev. B **75**, 155113 (2007).

[43] E. Gull, A. J. Millis, A. I. Lichtenstein, A. N. Rubtsov, M. Troyer, and P. Werner, Rev. Mod. Phys. **83**, 349 (2011).

[44] P. Sémon, C.-H. Yee, K. Haule, and A.-M. S. Tremblay, Phys. Rev. B **90**, 075149 (2014).

[45] M. Jarrell and J. Gubernatis, Phys. Rep. **269**, 133 (1996).

[46] J. H. Shim, K. Haule, and G. Kotliar, Science **318**, 1615 (2007).

[47] H. C. Choi, B. I. Min, J. H. Shim, K. Haule, and G. Kotliar, Phys. Rev. Lett. **108**, 016402 (2012).

[48] E. Gull, P. Werner, X. Wang, M. Troyer, and A. J. Millis, Europhys. Lett. **84**, 37009 (2008).

[49] A. Koga, N. Kawakami, T. M. Rice, and M. Sigrist, Phys. Rev. Lett. **92**, 216402 (2004).

[50] L. Huang, Y. Wang, and X. Dai, Phys. Rev. B **85**, 245110 (2012).

[51] E. R. Ylvisaker, J. Kuneš, A. K. McMahan, and W. E. Pickett, Phys. Rev. Lett. **102**, 246401 (2009).

[52] P. Werner and A. J. Millis, Phys. Rev. Lett. **99**, 126405 (2007).

[53] J. H. Shim, K. Haule, and G. Kotliar, Europhys. Lett. **85**, 17007 (2009).

[54] Here, $n_{5/2}$ and $n_{7/2}$ are evaluated using Matsubara Green's function $G(i\omega_n)$. The sum $(n_{5f} = n_{5/2} + n_{7/2})$ is somewhat smaller than that calculated from $\sum_\Gamma p_\Gamma N_\Gamma$.

[55] V. I. Anisimov, J. Zaanen, and O. K. Andersen, Phys. Rev. B **44**, 943 (1991).

[56] V. I. Anisimov and O. Gunnarsson, Phys. Rev. B **43**, 7570 (1991).

[57] O. Gunnarsson, O. K. Andersen, O. Jepsen, and J. Zaanen, Phys. Rev. B **39**, 1708 (1989).

[58] M. Cococcioni and S. de Gironcoli, Phys. Rev. B **71**, 035105 (2005).

[59] F. Aryasetiawan, M. Imada, A. Georges, G. Kotliar, S. Biermann, and A. I. Lichtenstein, Phys. Rev. B **70**, 195104 (2004).

[60] F. Aryasetiawan, K. Karlsson, O. Jepsen, and U. Schönberger, Phys. Rev. B **74**, 125106 (2006).

[61] B. Amadon, T. Applencourt, and F. Bruneval, Phys. Rev. B **89**, 125110 (2014).

[62] B. Amadon, Phys. Rev. B **94**, 115148 (2016).

[63] X. Gonze, F. Jollet, F. A. Araujo, D. Adams, B. Amadon, T. Applencourt, C. Audouze, J.-M. Beuken, J. Bieder, A. Bokhanchuk, E. Bousquet, F. Bruneval, D. Caliste, M. Côté, F. Dahm, F. D. Pieve, M. Delaveau, M. D. Gennaro, B. Dorado, C. Espejo, G. Geneste, L. Genovese, A. Gerossier, M. Giantomassi, Y. Gillet, D. Hamann, L. He, G. Jomard, J. L. Janssen, S. L. Roux, A. Levitt, A. Lherbier, F. Liu, I. Lukačević, A. Martin, C. Martins, M. Oliveira, S. Poncé, Y. Pouillon, T. Rangel, G.-M. Rignanese, A. Romero, B. Rousseau, O. Rubel, A. Shukri, M. Stankovski, M. Torrent, M. V. Setten, B. V. Troeye, M. Verstraete, D. Waroquiers, J. Wiktor, B. Xu, A. Zhou, and J. Zwanziger, Comput. Phys. Commun. **205**, 106 (2016).

[64] M. Torrent, F. Jollet, F. Bottin, G. Zérah, and X. Gonze, Comput. Mater. Sci. **42**, 337 (2008).

[65] P. E. Blöchl, Phys. Rev. B **50**, 17953 (1994).

[66] N. Holzwarth, A. Tackett, and G. Matthews, Comput. Phys. Commun. **135**, 329 (2001).

[67] We notice that pseudopotentials are not available for most of the actinide elements, especially the late actinides. Therefore, as a by-product of this project, we tried to generate a complete set of projector augmented-wave data sets for all of the actinide elements (from ^{89}Ac to ^{103}Lr). They have been uploaded to GitHub (see https://github.com/huangli712/hpaw). We hope that our contribution will benefit the whole community of actinide research.